



## Room acoustics simulation using 3-D compact explicit FDTD schemes

Kowalczyk, K., & Van Walstijn, M. (2011). Room acoustics simulation using 3-D compact explicit FDTD schemes. *IEEE TRANSACTIONS ON AUDIO SPEECH AND LANGUAGE PROCESSING*, 19(1), 34-46. [5440917]. DOI: 10.1109/TASL.2010.2045179

### Published in:

IEEE TRANSACTIONS ON AUDIO SPEECH AND LANGUAGE PROCESSING

### Document Version:

Peer reviewed version

### Queen's University Belfast - Research Portal:

[Link to publication record in Queen's University Belfast Research Portal](#)

### General rights

Copyright for the publications made accessible via the Queen's University Belfast Research Portal is retained by the author(s) and / or other copyright owners and it is a condition of accessing these publications that users recognise and abide by the legal requirements associated with these rights.

### Take down policy

The Research Portal is Queen's institutional repository that provides access to Queen's research output. Every effort has been made to ensure that content in the Research Portal does not infringe any person's rights, or applicable UK laws. If you discover content in the Research Portal that you believe breaches copyright or violates any law, please contact [openaccess@qub.ac.uk](mailto:openaccess@qub.ac.uk).

# Room acoustics simulation using 3-D compact explicit FDTD schemes

Konrad Kowalczyk\* and Maarten van Walstijn

**Abstract**—This paper presents methods for simulating room acoustics using the finite-difference time-domain (FDTD) technique, focusing on boundary and medium modeling. A family of nonstaggered 3-D compact explicit FDTD schemes is analyzed in terms of stability, accuracy, and computational efficiency, and the most accurate and isotropic schemes based on a rectilinear grid are identified. A frequency-dependent boundary model that is consistent with locally reacting surface theory is also presented, in which the wall impedance is represented with a digital filter. For boundaries, accuracy in numerical reflection is analyzed and a stability proof is provided. The results indicate that the proposed 3-D interpolated wideband and isotropic schemes outperform directly related techniques based on Yee’s staggered grid and standard digital waveguide mesh, and that the boundary formulations generally have properties that are similar to that of the basic scheme used.

**Index Terms**—Acoustic propagation, acoustic reflection, acoustic signal processing, architectural acoustics, finite-difference time-domain (FDTD) methods, numerical analysis.

## I. INTRODUCTION

OVER the past two decades, various computer modeling techniques have been developed for auralization and room acoustic purposes, with the main applications being spatialization of sound or speech, computer games, and architectural design tools [1], [2], [3], [4]. The level of accuracy to which the sound environment is modeled depends strongly on the application and availability of computational resources for audio signal processing. In room acoustics modeling, two distinct approaches dominate, namely geometrical and wave-based methods. In general, geometrical techniques (see, e.g., [5], [6], [7], [3], [8]) are more efficient but the underlying assumption of approximating sound waves with sound rays is justified for high frequencies only [9]. In contrast, wave-based methods, that inherently model all wave-related phenomena, are typically accurate at lower frequencies. Accurate room acoustics prediction and auralization thus requires using the wave-based method at high sample rates or hybrid models that apply the two different approaches for different frequency bands [10].

Manuscript received October 22, 2009; revised December 23, 2009. The associate editor coordinating the review of this manuscript and approving it for publication was Prof. Vesa Välimäki.

K. Kowalczyk performed this work while at the Sonic Arts Research Centre, Queen’s University, Belfast, UK. He is now with Multimedia Communication and Signal Processing (LMS), University of Erlangen-Nuremberg, Cauerstr. 7, 91058 Erlangen, Germany e-mail: (kowalczyk@lnt.de)

M. van Walstijn is with the Sonic Arts Research Centre (SARC) and the School of Electronics, Electrical Engineering and Computer Science, Queen’s University, Belfast, United Kingdom BT7 1NN e-mail: (m.vanwalstijn@qub.ac.uk)

Digital Object Identifier T-ASL-02592-2009.

Among wave-based methods, finite-differences are usually applied in the form of Yee’s staggered scheme [11], originally employed in the room acoustics domain by Botteldooren in [4],[12]. Obtaining accurate predictions with Yee’s scheme requires heavy oversampling to reduce the numerical dispersion error, which leads to enormous computational costs. The efficiency can in principle be improved using implicit schemes to reduce the dispersion error, thereby allowing the use of a much lower sample rate [13], [14], but the implementation and boundary formulations for irregular room geometries present major difficulties for such schemes. Improving accuracy is also possible using higher-order spatial schemes (known as ‘large star’ systems), but then the treatment of boundaries becomes unwieldy. For this reason, this paper considers only compact explicit FDTD schemes, aiming to identify those schemes within that family that are the most efficient for modeling of acoustic systems in a specified audio bandwidth. In addition, considerations are constrained here to nonstaggered 3-D compact schemes on a rectilinear stencil, allowing a straightforward fit of the grid to enclosures with mainly parallel walls, which are predominant in real architecture.

Our formulation of the family of compact explicit schemes captures many schemes proposed in previous studies, including the standard leapfrog (SLF) scheme [15], the octahedral scheme [16], [17], [18], and the 3-D interpolated digital waveguide mesh (IDWM) [19]. Note that in general the digital waveguide mesh (DWM) can be considered as a subclass of FDTD methods, hence the FDTD schemes and waveguides based on the same stencil are mathematically equivalent [20], e.g., the 3-D SLF scheme [15] is equivalent to the 3-D rectilinear DWM [21], and the tetrahedral scheme is equivalent to the tetrahedral DWM. In comparison to previous studies that have investigated schemes on 3-D grid topologies ([16],[17],[18]), our approach differs mainly in the way that numerical dispersion is viewed not as a function of wavenumbers, but directly as a function of frequency and propagation direction (such as in [22], [23]). This new way of looking at schemes leads to different conclusions, including the identification of novel schemes such as the interpolated isotropic schemes and the interpolated wideband scheme.

Many boundary terminations used in DWM simulations employ a reflection coefficient or reflection filter directly attached to a single system port (see, e.g., [24], [25], [26], [27]). The same one-dimensional solution to what is fundamentally a two-dimensional problem appears to have been applied in [28] for modeling frequency-dependent boundaries in Yee’s FDTD scheme. As explained in [29], [30], [23], this simplification is unphysical, and it has been shown in [29], [30] that large

reflection errors and instabilities may result for this approach. In this paper, a general approach to formulating the digital impedance filter (DIF) boundary model (originally proposed in [30] for the 2-D SLF scheme) for all discussed 3-D FDTD schemes is presented, and the analysis of reflection magnitude for various cases is provided.

The paper is organized as follows. In Section II the general formulation of the 3-D compact explicit scheme is presented, and a detailed analysis of the numerical stability, dispersion error, isotropy and accuracy of special cases is provided. A general formulation of the 3-D compact explicit DIF model (including numerical reflection analysis and stability proof) is presented in Section III, followed by general conclusions in Section IV.

## II. MEDIUM MODELING

In room acoustics, the medium through which sound waves travel is air. Considering a 3-D Cartesian coordinate system  $x$ - $y$ - $z$ , sound wave propagation in air is governed by

$$\frac{\partial^2 p}{\partial t^2} = c^2 \left( \frac{\partial^2 p}{\partial x^2} + \frac{\partial^2 p}{\partial y^2} + \frac{\partial^2 p}{\partial z^2} \right), \quad (1)$$

where  $p$  is the acoustic pressure variable and  $c$  is the sound wave velocity. Any compact explicit scheme approximating the continuous 3-D wave equation (1) can be described by

$$\begin{aligned} \delta_t^2 p_{l,m,i}^n &= \lambda^2 \left[ (\delta_x^2 + \delta_y^2 + \delta_z^2) \right. \\ &\quad \left. + a (\delta_x^2 \delta_y^2 + \delta_y^2 \delta_z^2 + \delta_x^2 \delta_z^2) \right. \\ &\quad \left. + b \delta_x^2 \delta_y^2 \delta_z^2 \right] p_{l,m,i}^n, \end{aligned} \quad (2)$$

where  $a$  and  $b$  denote two free numerical parameters,  $p_{l,m,i}^n$  is the update variable, and  $l$ ,  $m$ , and  $i$  denote spatial indexes in  $x$ -,  $y$ -, and  $z$ -direction, respectively.  $\lambda = cT/X$  denotes the Courant number, where  $X$  is the grid spacing and  $T = 1/f_s$  is the time step. Applying the second-order derivative centered finite-difference operators  $\delta_t^2$ ,  $\delta_x^2$ ,  $\delta_y^2$ , and  $\delta_z^2$ , defined as

$$p_{l,m,i}^n \equiv p(x, y, z, t) \Big|_{x=lX, y=mX, z=iX, t=nT}, \quad (3)$$

$$\delta_t^2 p_{l,m,i}^n \equiv p_{l,m,i}^{n+1} - 2p_{l,m,i}^n + p_{l,m,i}^{n-1}, \quad (4)$$

$$\delta_x^2 p_{l,m,i}^n \equiv p_{l+1,m,i}^n - 2p_{l,m,i}^n + p_{l-1,m,i}^n, \quad (5)$$

$$\delta_y^2 p_{l,m,i}^n \equiv p_{l,m+1,i}^n - 2p_{l,m,i}^n + p_{l,m-1,i}^n, \quad (6)$$

$$\delta_z^2 p_{l,m,i}^n \equiv p_{l,m,i+1}^n - 2p_{l,m,i}^n + p_{l,m,i-1}^n, \quad (7)$$

to (2) yields the generalized difference equation for compact explicit schemes:

$$\begin{aligned} p_{l,m,i}^{n+1} &= d_1 (p_{l+1,m,i}^n + p_{l-1,m,i}^n + p_{l,m+1,i}^n + p_{l,m-1,i}^n \\ &\quad + p_{l,m,i+1}^n + p_{l,m,i-1}^n) + d_2 (p_{l+1,m+1,i}^n + p_{l+1,m-1,i}^n \\ &\quad + p_{l+1,m,i+1}^n + p_{l+1,m,i-1}^n + p_{l-1,m+1,i}^n + p_{l-1,m-1,i}^n \\ &\quad + p_{l-1,m,i+1}^n + p_{l-1,m,i-1}^n + p_{l-1,m+1,i}^n + p_{l-1,m-1,i}^n \\ &\quad + p_{l-1,m,i+1}^n + p_{l-1,m,i-1}^n) + d_3 (p_{l+1,m+1,i+1}^n \\ &\quad + p_{l+1,m-1,i+1}^n + p_{l+1,m+1,i-1}^n + p_{l+1,m-1,i-1}^n \\ &\quad + p_{l-1,m+1,i+1}^n + p_{l-1,m-1,i+1}^n + p_{l-1,m+1,i-1}^n \\ &\quad + p_{l-1,m-1,i-1}^n) + d_4 p_{l,m}^n - p_{l,m}^{n-1}, \end{aligned} \quad (8)$$

with the coefficients

$$\begin{aligned} d_1 &= \lambda^2 (1 - 4a + 4b), \quad d_2 = \lambda^2 (a - 2b), \\ d_3 &= \lambda^2 b, \quad \text{and} \quad d_4 = 2(1 - 3\lambda^2 + 6\lambda^2 a - 4b\lambda^2). \end{aligned} \quad (9)$$

The free parameters  $a$  and  $b$  determine the specific characteristics of the scheme. A list of schemes with their respective implementation coefficient values and further properties is presented in Table I.

### A. Stability Analysis

Investigating the numerical stability of FDTD schemes amounts to ensuring that no growing solutions of the numerical system exist [15], [31]. For analysis of linear systems, single-frequency plane-wave solutions may be assumed, as for example in von Neumann analysis [31]). Consider such a plane wave traveling in positive  $x$ -direction of a 3-D coordinate system  $x$ - $y$ - $z$ , and cutting the Cartesian  $x$ -axis at a pair of angles  $(\theta, \phi)$ , where  $\theta$  and  $\phi$  denote the azimuth and elevation angles, respectively

$$p(x, y, z, t) = p_0 e^{st} e^{-jk_x x} e^{-jk_y y} e^{-jk_z z}, \quad (10)$$

where  $p_0$  denotes the amplitude,  $s = \sigma + j\omega$  denotes complex frequency,  $k$  is the continuous-time wavenumber, and  $k_x = k \cos \theta \cos \phi$ ,  $k_y = k \sin \theta \cos \phi$ , and  $k_z = k \sin \phi$ . In the discrete space-time domain, the plane wave takes the form

$$p_{l,m,i}^n = p_0 e^{snT} e^{-j\hat{k}_x lX} e^{-j\hat{k}_y mX} e^{-j\hat{k}_z iX}, \quad (11)$$

where the directional numerical wavenumbers are related to the wavenumber in a propagation direction by  $\hat{k}^2 = \hat{k}_x^2 + \hat{k}_y^2 + \hat{k}_z^2$ , and are respectively given as  $\hat{k}_x = \hat{k} \cos \theta \cos \phi$ ,  $\hat{k}_y = \hat{k} \sin \theta \cos \phi$ , and  $\hat{k}_z = \hat{k} \sin \phi$ . For solutions of this kind, the centered finite-difference operators defined in (4-7) can be written as

$$\begin{aligned} \delta_t^2 p_{l,m,i}^n &= (z - 2 + z^{-1}) p_{l,m,i}^n \\ &= -4 \sin^2(\omega T/2) p_{l,m,i}^n, \end{aligned} \quad (12)$$

$$\delta_x^2 p_{l,m,i}^n = -4 \sin^2(\hat{k}_x X/2) p_{l,m,i}^n, \quad (13)$$

$$\delta_y^2 p_{l,m,i}^n = -4 \sin^2(\hat{k}_y X/2) p_{l,m,i}^n, \quad (14)$$

$$\delta_z^2 p_{l,m,i}^n = -4 \sin^2(\hat{k}_z X/2) p_{l,m,i}^n, \quad (15)$$

where  $z = e^{sT}$  represents the classic relationship in DSP literature between  $s$ - and  $z$ -domains. Substituting (12-15) into (2), the following amplification equation results

$$z + 2B(s_x, s_y, s_z) + z^{-1} = 0, \quad (16)$$

where

$$B(s_x, s_y, s_z) = 2\lambda^2 F(s_x, s_y, s_z) - 1, \quad (17)$$

and

$$\begin{aligned} F(s_x, s_y, s_z) &= (s_x + s_y + s_z) - 4a(s_x s_y + s_x s_z + s_y s_z) \\ &\quad + 16bs_x s_y s_z, \end{aligned} \quad (18)$$

where the new variables are respectively defined as  $s_x = \sin^2(\hat{k}_x X/2)$ ,  $s_y = \sin^2(\hat{k}_y X/2)$ , and  $s_z = \sin^2(\hat{k}_z X/2)$ . From the  $z$ -transform shift theorem the update variable can be written as  $p_{l,m}^{n+1} = z p_{l,m}^n$ , and thus the necessary stability

condition for a FDTD scheme yields  $|z| \leq 1$ . Consequently, the moduli of the solutions to the amplification polynomial (16) have to be smaller than or equal to unity for any combination  $(s_x, s_y, s_z)$ . Considering real-valued wavenumbers only in the range  $-\pi/X \leq \hat{k}_x, \hat{k}_y, \hat{k}_z \leq \pi/X$ , the stability condition  $|z| \leq 1$  leads to the following bound on the Courant number

$$\lambda^2 \leq \frac{1}{F(s_x, s_y, s_z)}, \quad (19)$$

which has to hold for all possible values of  $s_x, s_y, s_z$ . The nature of the function  $F$  is such that its maximum value  $F_{\max}$  always occurs at one of the extrema in the domain  $s_x, s_y, s_z \in [0, 1]$ , from which it can be deduced that

$$F_{\max} = \max(1, 2 - 4a, 3 - 12a + 16b), \quad (20)$$

hence the stability condition for the 3-D compact explicit FDTD schemes is

$$\lambda^2 \leq \min\left(1, \frac{1}{2 - 4a}, \frac{1}{3 - 12a + 16b}\right). \quad (21)$$

Since  $\lambda^2$  can only be positive, the domain of the free parameters is ultimately reduced to

$$a \leq \frac{1}{2}, \quad b \geq \frac{1}{16}(12a - 3). \quad (22)$$

Thus stable a 3-D compact explicit schemes results for any set of parameters  $(a, b)$  that satisfy (22), and the resulting stability condition on the Courant number follows from (21).

### B. Numerical Dispersion

An unwanted side effect of the FDTD technique is that numerical dispersion error is introduced, resulting in high frequency waves traveling at a lower speed than  $c$ . It is common to express this error in terms of the relative phase velocity that is defined as the ratio of the effective numerical wave speed  $\hat{c} = \omega/\hat{k}$  over the real wave speed  $c$  [16]. As shown in previous work [22] the dispersion relation of the numerical simulation can be derived directly from the amplification equation (16), and takes the form

$$\sin^2(\omega T/2) = \lambda^2 F(s_x, s_y, s_z). \quad (23)$$

Again following [22], frequency can be written explicitly as a function of the wavenumbers, from which the relative phase velocity can be deduced. In the 3D case, this procedure yields

$$v(\hat{k}_x, \hat{k}_y, \hat{k}_z) = \frac{\omega}{\hat{k}c} = \frac{2 \arcsin\left(\lambda \sqrt{F(s_x, s_y, s_z)}\right)}{\lambda \sqrt{(\hat{k}_x X)^2 + (\hat{k}_y X)^2 + (\hat{k}_z X)^2}}. \quad (24)$$

### C. Cutoff frequency

As shown in [16], [22]), the largest numerical error always occurs in one of extreme directions, which in a 3-D case are defined as the axial ( $\theta = 0^\circ, \phi = 0^\circ$ ), the side-diagonal ( $\theta = 45^\circ, \phi = 0^\circ$ ), and the diagonal ( $\theta = 45^\circ, \phi = 35^\circ$ ) directions. Thus we refer to the side-diagonal direction when considering the diagonal of the side of a cube, and to the diagonal direction when considering the diagonal of a cube. Inserting (18) for a

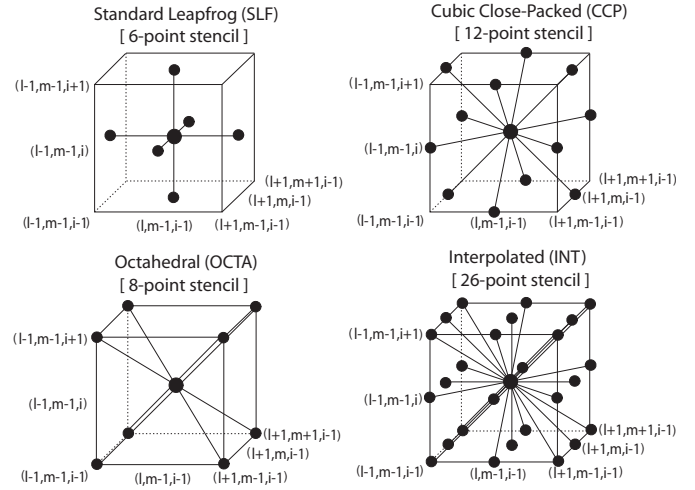


Fig. 1. Compact FDTD stencils for the standard leapfrog, octahedral, cubic close-packed, and interpolated schemes.

given direction into (23), solving for  $\hat{k}$ , and finally noting that the function  $f(x) = \arcsin(x)$  becomes complex-valued for  $x > 1$ , the cutoff frequency for a given direction is obtained. For axial, side-diagonal, and diagonal directions these cutoff frequencies are respectively given as

$$\begin{aligned} f_a T &= \frac{\arcsin(\lambda)}{\pi}, \\ f_{sd} T &= \frac{\arcsin(\lambda \sqrt{2 - 4a})}{\pi}, \\ f_d T &= \frac{\arcsin(\lambda \sqrt{3 - 12a + 16b})}{\pi}. \end{aligned} \quad (25)$$

### D. Special Cases of 3-D Compact Explicit Schemes

The most important 3-D compact explicit schemes based on a rectilinear grid are presented in Table I, which provides information about the number of neighbouring points used in an update formula, the values of free parameters  $(a, b)$ , the stability bound on the Courant number, the values of coefficients used in implementation ( $d_1, d_2, d_3$ , and  $d_4$ ), and the cutoff frequencies in axial  $f_a T$ , side-diagonal  $f_{sd} T$ , and diagonal  $f_d T$  directions. Note that setting the Courant number at its maximum value is in general the best choice as it yields the smallest dispersion error and the widest bandwidth [29].

The standard leapfrog scheme (SLF) has a stencil that consists of 6 neighboring nodes in axial directions only, as depicted in Fig. 1. At the top value of the Courant number, the SLF scheme has the same numerical dispersion and stability properties as the 3-D Yee's scheme based on a staggered grid (applied, e.g., in [4]) and the rectilinear digital waveguide mesh (DWM) [32]. Furthermore, the reader is reminded that the 3-D rectilinear DWM implementation using Kirchhoff variables is identical to the implementation of the SLF scheme with  $\lambda = \sqrt{1/3}$ . The scheme that utilizes 8 neighboring nodes in diagonal directions only (see Fig. 1) is referred to in FDTD and DWM literature as the octahedral (OCTA) scheme [16], [17], [18], [19]. The cubic close-packed (CCP) scheme [17], [18], [19] uses 12 spatial grid points in an update formula,

TABLE I  
3D COMPACT EXPLICIT SCHEMES, WHERE  $f_a T$ ,  $f_{sd} T$  AND  $f_d T$  DENOTE THE CUTOFF FREQUENCIES IN AXIAL, SIDE-DIAGONAL AND DIAGONAL DIRECTIONS, RESPECTIVELY.

	Standard Leapfrog (SLF)	Octahedral (OCTA)	Cubic Close-Packed (CCP)	Interp. DWM (IDWM)	Interp. Isotropic (IISO)	Isotropic 2 (IISO2)	Interp. Wideband (IWB)
nr grid points	6	8	12	26	18	26	26
$a$	0	$\frac{1}{2}$	$\frac{1}{4}$	0.2034	$\frac{1}{6}$	$\frac{1}{6}$	$\frac{1}{4}$
$b$	0	$\frac{1}{4}$	0	0.0438	0	$\frac{1}{48}$	$\frac{1}{16}$
$\lambda$	$\sqrt{\frac{1}{3}}$	1	1	$\sqrt{\frac{1}{3}}$	$\sqrt{\frac{3}{4}}$	$\sqrt{\frac{3}{4}}$	1
$d_1$	$\frac{1}{3}$	0	0	0.1205	$\frac{1}{4}$	$\frac{15}{48}$	$\frac{1}{4}$
$d_2$	0	0	$\frac{1}{4}$	0.0386	$\frac{1}{4}$	$\frac{1}{32}$	$\frac{1}{8}$
$d_3$	0	$\frac{1}{4}$	0	0.0146	0	$\frac{1}{64}$	$\frac{5}{8}$
$d_4$	0	0	-1	0.6970	-1	$-\frac{1}{8}$	$-\frac{3}{2}$
$f_a T$	0.196	0.5	0.5	0.196	0.333	0.333	0.5
$f_{sd} T$	0.304	0.25	0.5	0.216	0.5	0.5	0.5
$f_d T$	0.5	0.25	0.333	0.225	0.377	0.5	0.5
bandwidth	0.196	0.25	0.333	0.196	0.333	0.333	0.5
accuracy (2%)	0.075	0.093	0.175	0.069	0.175	0.175	0.186
isotropy (2%)	0.075	0.093	0.175	0.191	0.269	0.269	0.186

as illustrated in Fig. 1. The remaining schemes are referred to as ‘interpolated schemes’ [16], and they can be viewed as a linear superposition of three stencils, namely the standard leapfrog, octahedral, and cubic close-packed schemes. For most cases its implementation uses all 26 nearest neighboring grid points surrounding the updated point, as depicted in Fig. 1. A nearly direction-independent dispersion error is obtained for the following pairs of coefficients: ( $a = 1/6$ ,  $b = 0$ ), ( $a = 1/6$ ,  $b = 1/48$ ), and ( $a = 1/6$ ,  $b = -1/16$ ). These schemes are thus referred to as 3-D interpolated isotropic schemes with the respective abbreviations given as IISO, IISO2, and IISO3. Note that for IISO2 and IISO3 not all surrounding grid points are used in an update. These three schemes have similar characteristics, and hence the results for the IISO3 are omitted here for brevity. In [19], the coefficients of the 3-D interpolated digital waveguide mesh (IDWM) have been calculated using an optimization method up to  $0.25f_s$ . The coefficients presented in [19] are equivalent to setting  $a = 0.2034$ ,  $b = 0.0438$  and  $\lambda = 0.5773$  in (8). In contrast to the 2-D case [23], these coefficients are not close to the coefficients of the 3-D isotropic schemes. As can be seen from Table I, the only scheme that provides the whole available bandwidth (i.e., up to the Nyquist frequency) in all propagation directions is the 3-D interpolated wideband scheme (IWB).

#### E. Accuracy and Isotropy Analysis

The most informative way of inspecting the dispersion error is to plot the relative phase velocity for those directions in which the largest and the smallest dispersion consistently occurs [22]. The results for the axial, side-diagonal, and

diagonal directions only are illustrated in Fig. 2, and Fig. 3 illustrates the absolute value of the difference between the relative phase velocity for two extreme directions (having the lowest and the highest dispersion error respectively).

In interpreting these results, let us first investigate the frequency range in which the simulation is considered valid, which is determined by the lowest cutoff frequency (of all directions). As can be seen from Table I, and Fig. 2, the SLF and the IDWM<sup>1</sup> have the lowest cutoff in axial directions which reduces their valid frequency range to  $0.196f_s$ . The OCTA scheme has the lowest cutoff frequencies in side-diagonal and diagonal directions, which limits its valid frequency range to  $0.25f_s$ . The CCP and all three interpolated isotropic schemes produce valid results for up to  $0.33f_s$ . The only scheme that uses the whole available bandwidth (i.e., up to  $0.5f_s$ ) is the IWB scheme.

In terms of accuracy within the model bandwidth, Fig. 2 shows that the 3-D SLF scheme (and thus the 3-D rectilinear DWM and 3-D Yee’s staggered scheme) displays no numerical dispersion in diagonal directions, but suffers from a large errors for axial propagation directions. On the other hand, the IWB, CCP, and OCTA schemes display no error in axial directions, but the latter two are generally showing a larger error in the other two propagation directions than the IWB. In order to capture these effects in a single quantity, let us define the accuracy criterion as a frequency band in which

<sup>1</sup>The reader is reminded that the spectrum is enlarged to a wider valid frequency range after the warping technique is applied. In fact, the presented coefficients of the IDWM have been optimized for the after-warping cutoff frequency of  $0.25f_s$  [19].

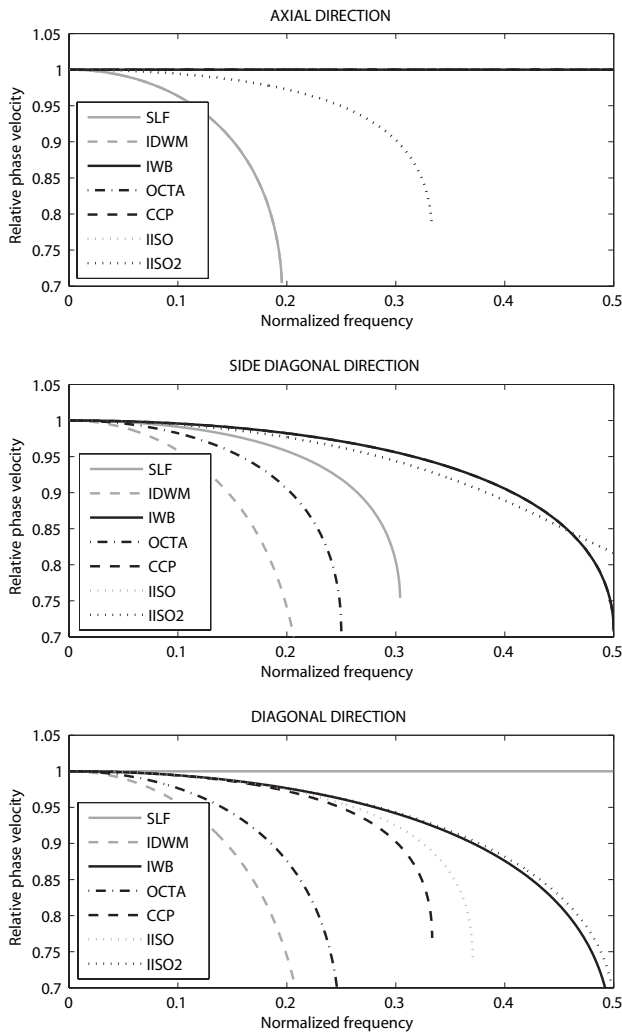


Fig. 2. Relative phase velocity of compact 3D schemes for axial (top), side-diagonal (middle), and diagonal directions (bottom), respectively. Note that in the top plot, the relative phase velocity of the following groups (IWB,OCTA,CCP), (IISO,IISO2), and (SLF,IDWM) overlap, respectively.

the maximum relative numerical error does not exceed 2%. A similar criterion can be applied to isotropy, where the admissible isotropy error between the two extreme propagation directions is limited to 2%. As depicted in Figs. 2 and 3, the SLF scheme (and thus also the DWM and the Yee's scheme) is considered accurate under this definition for up to  $0.075f_s$ . The OCTA scheme is accurate for up to  $0.093f_s$ , and for the same frequency range it is also considered isotropic. The CCP scheme has a wider frequency range of accuracy which spreads up to  $0.175f_s$ , which also coincides with the isotropy range. The accuracy bandwidth of the IDWM scheme (before warping) is reduced to  $0.069f_s$ . Applying the 2% criterion, the IDWM is considered isotropic up to  $0.191f_s$ . The IISO and the IISO2 schemes have their accuracy frequency ranges that extend to  $0.175f_s$ , the same as for the CCP scheme. The range of frequencies for which the IISO and the IISO2 are considered isotropic reaches as far as  $0.269f_s$ , considerably

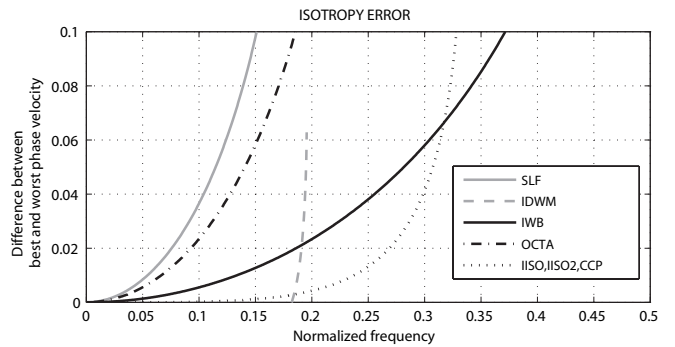


Fig. 3. The absolute value of the difference between the relative phase velocity in two extreme directions of 3D compact schemes. Note that IISO, IISO2, and CCP overlap.

further than the IDWM<sup>2</sup>. Finally, the IWB scheme is accurate for up to  $0.186f_s$ , which is also its isotropy range.

#### F. Spectral Analysis of the Room Impulse Response

The impact of the dispersion error present in the numerically measured room impulse response (RIR) on theoretical room modes is investigated using the eigenmode model for rigid boundaries [9]. A cubic room of a constant size is modeled using  $7 \times 7 \times 7$ ,  $9 \times 9 \times 9$ , and  $12 \times 12 \times 12$  nodes for schemes respectively having the stability bound at  $\lambda = 1/\sqrt{3}$ ,  $\sqrt{3}/4$ , and 1, where excitation and pickup points are located near opposite corners and the boundary nodes are kept at 0 (i.e., fixed boundaries) in order to make sure that no additional error is introduced by the boundary.

As illustrated in Fig. 4, as a general tendency at low frequencies, modes are systematically shifted down, and this artefact becomes larger with increasing frequency. The RIR for the SLF model exhibits a significantly reduced number of room modes, while the RIRs for the OCTA and the CCP room models are characterized by an increased modal density around their lowest cutoff frequencies (i.e.,  $0.25f_s$  and  $0.33f_s$ , respectively). Furthermore, the SLF and OCTA spectra are symmetric about their lowest cutoff frequency ( $0.25f_s$ ), which re-inforces the notion that the system response is invalid above the lowest numerical cut-off. The IDWM model displays a strongly compressed spectrum, much more so than IISO and IISO2. The most accurate match at low frequencies results for the IWB model. Although its lowest cutoff falls at  $0.5f_s$ , the spectrum does display a gradual increase of modal density, effectively 'pulling in' modes from above the Nyquist frequency.

#### G. Computational Cost

In simulations of room acoustics one typically requires a predefined accuracy (e.g., 2%) within a specified bandwidth. Thus a suitable metric for computational costs is the amount of computation required in order to obtain a specified accuracy

<sup>2</sup>However, it has to be remembered here that the main advantage of the IDWM is that it is nearly completely directionally-independent up to  $0.18f_s$ , enabling a highly precise recovery of any components within this bandwidth via frequency warping.

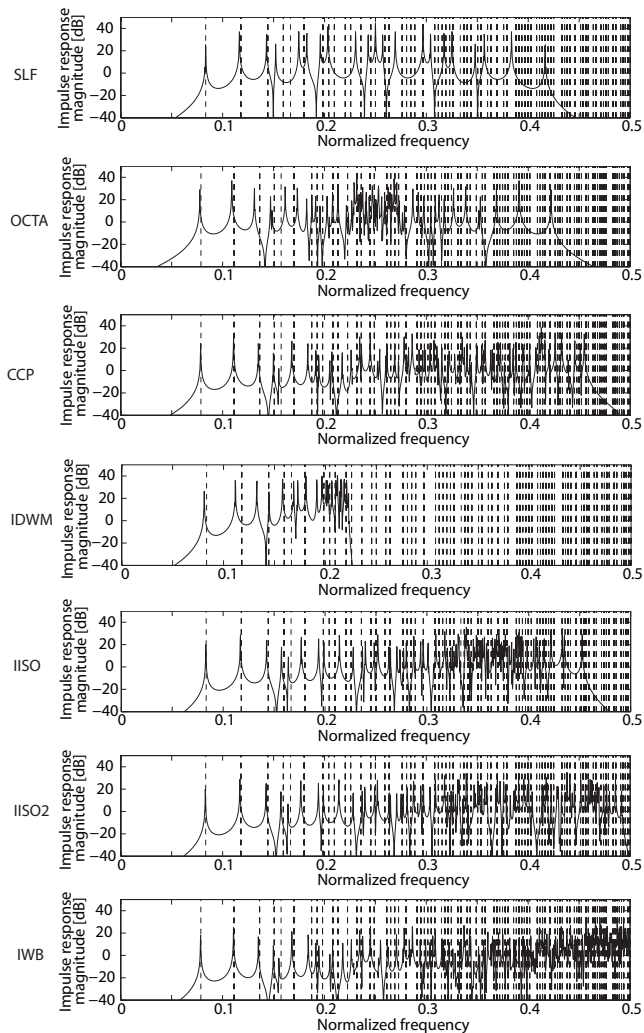


Fig. 4. Magnitude of the impulse response of the room with fixed boundaries as calculated with each of the presented schemes. Dashed lines denote the ideal mode frequencies of the room.

over a certain bandwidth. Analogous to [22], we can define the computational density as the number of nodal updates per cubic meter per second as  $\rho_{nu} = f_s/X^3$ , where  $f_s$  is the sampling frequency required to guarantee accurate simulation (i.e., in which the relative dispersion error does not exceed  $e_c$  in any propagation direction), and  $X$  denotes the grid spacing calculated from the Courant number as  $X = c/(f_s\lambda)$ . The required sample rate is calculated as  $f_s = \omega_c / \min(\omega_a T, \omega_{sd} T, \omega_d T)$  for the minimum normalized frequency in axial, side-diagonal, and diagonal propagation directions for which the accuracy is ensured.  $\omega_c$  can be set arbitrarily and it has to be applied consistently for calculating the computational density  $\rho_{nu}$  of all compared schemes. Finally, the relative efficiency is defined as

$$\varepsilon(a, b, e_c) = \frac{\rho_{nu}(0, 0, e_c, \omega_c)}{\rho_{nu}(a, b, e_c, \omega_c)} \quad (26)$$

so that  $\varepsilon(a, b, e_c)$  is independent of the choice of  $\omega_c$  and the resulting value is normalized by the computational density of the SLF scheme. The results of such a computational analysis for all cases of 3-D compact explicit schemes at their top

TABLE II  
RELATIVE COMPUTATIONAL EFFICIENCY FOR SPECIAL CASES OF 3D  
COMPACT EXPLICIT SCHEMES.

	SLF	OCTA	CCP	IDWM	IISO(2)	IWB
$\lambda$	$\sqrt{\frac{1}{3}}$	1	1	$\sqrt{\frac{1}{3}}$	$\sqrt{\frac{3}{4}}$	1
$\varepsilon(2\%)$	1	0.44	5.63	0.7	8.67	7.01
$\varepsilon(4\%)$	1	0.44	4.65	0.73	7.14	7.07
$\varepsilon(8\%)$	1	0.44	3.46	0.8	5.31	6.99

Courant numbers and the following values of the relative critical error  $e_c = 2\%, 4\%, 8\%$  are presented in Table II. Note that all presented schemes require storing two pressure values per grid point.

This computation does not take into account the differences in the amount of arithmetic operations per nodal update. However, note that difference equation coefficients for the SLF, the OCTA, the CCP, the IISO, and the IWB schemes makes them particularly attractive for efficient fixed-point implementations since multiplications can be computed as bit shift operations. This is not the case for the IDWM and the IISO2 scheme (see Table I).

Results presented in Table II indicate that the IWB and both isotropic schemes (i.e., IISO and IISO2) are in general the most efficient among compact explicit schemes, and both have a significantly higher efficiency than the remaining schemes. In particular, IISO and IISO2 are the most efficient for a tight accuracy criterion (up to 4%), the IWB scheme has the lowest computational cost when low accuracy is sufficient (above 4%). On the other hand, the worst efficiency results for the OCTA scheme.

### III. BOUNDARY MODELING

In simulations of room acoustics, the boundary is typically assumed to be locally reacting, i.e., no waves propagate in the boundary itself along its surface. This simplification holds only for boundaries for which the particle velocity depends solely on the sound pressure in front of the wall, and not on the pressure of neighboring wall elements [9]. The continuous-time boundary condition suitable for application to nonstaggered FDTD schemes (i.e., in terms of pressure only) has been derived in [29], which for the right boundary of a 3-D coordinate system  $x$ - $y$ - $z$  yields

$$\frac{\partial p}{\partial t} = -c \xi_w \frac{\partial p}{\partial x}, \quad (27)$$

where  $\xi_w = Z_w/\rho c$  is the specific wall impedance, and  $\rho$  and  $Z_w$  are the air density and the boundary impedance, respectively. When both the boundary condition and the wave equation simultaneously apply at a boundary [29], the planar-wave reflection coefficient [9] may be defined as

$$R_{\theta, \phi}(z) = \frac{\xi_w(z) \cos \theta \cos \phi - 1}{\xi_w(z) \cos \theta \cos \phi + 1}. \quad (28)$$

In order to ensure that the designed impedance filter is positive real, it has been proposed in [30] to first design a digital

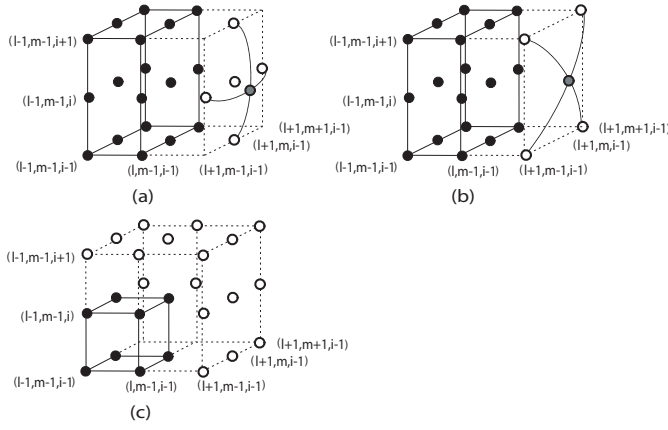


Fig. 5. The interpolated mesh at: (a,b) a right boundary and (c) a right-top corner. Room interior nodes are indicated with black-colored circles, ghost points are indicated with white-colored circles, and interpolated nodes are indicated with grey-colored circles.

reflection filter  $R_{0,0}(z)$  that matches reflection data for a normal angle of incidence, and next to obtain the digital impedance filter (DIF)  $\xi_w(z)$  from inverted (28) as

$$\xi_w(z) = \frac{1 + R_{0,0}(z)}{1 - R_{0,0}(z)}, \quad (29)$$

thus an impedance is always given as an IIR filter. This approach is well adapted to typically available reflection coefficient data for a normal incidence (conveniently converted in each octave band from the measured absorption coefficients  $\alpha$  averaged across all reflection directions by  $|R| = \sqrt{1 - \alpha}$ ), and additionally it guarantees that for a passive reflection filter a positive real impedance filter results [30].

### A. 3-D Compact Explicit Boundary Model

In this section, a method for constructing the boundary formulations for the general family of 3-D nonstaggered compact explicit FDTD schemes is proposed. In general, such a digital impedance filter (DIF) model is derived by combining the boundary condition in the direction normal to the boundary surface with the respective wave approximation. Considering a right boundary of a room modeled with a general 3-D scheme given by (8), there are nine grid points lying outside the modeled space, which in FDTD literature are often referred to as ‘ghost points’ [33]. These points should be eliminated from the wave equation using a general boundary condition, which for a general case (see Fig. 5(a-b)) is subdivided into three elimination steps: 1) for an axial ghost point, 2) for four side-diagonal ghost points, and 3) for four diagonal ghost points. We first apply a linear interpolation on side-diagonal grid points lying inside and outside of the modeled space (as depicted in Fig. 5(a)), which can be expressed as

$$\tilde{p}_{l-1,m,i}^n = \frac{1}{4}(p_{l-1,m+1,i}^n + p_{l-1,m-1,i}^n + p_{l-1,m,i+1}^n + p_{l-1,m,i-1}^n), \quad (30)$$

$$\tilde{p}_{l+1,m,i}^n = \frac{1}{4}(p_{l+1,m+1,i}^n + p_{l+1,m-1,i}^n + p_{l+1,m,i+1}^n + p_{l+1,m,i-1}^n), \quad (31)$$

where  $\tilde{p}_{l-1,m,i}^n$  and  $\tilde{p}_{l+1,m,i}^n$  are the pressure values at two interpolated nodes lying on the sphere that goes through all eight side-diagonal ghost points. An analogous interpolation of diagonal inner and outer grid nodes yields

$$\bar{p}_{l-1,m,i}^n = \frac{1}{4}(p_{l-1,m+1,i+1}^n + p_{l-1,m-1,i+1}^n + p_{l-1,m+1,i-1}^n + p_{l-1,m-1,i-1}^n), \quad (32)$$

$$\bar{p}_{l+1,m,i}^n = \frac{1}{4}(p_{l+1,m+1,i+1}^n + p_{l+1,m-1,i+1}^n + p_{l+1,m+1,i-1}^n + p_{l+1,m-1,i-1}^n), \quad (33)$$

where  $\bar{p}_{l-1,m,i}^n$  and  $\bar{p}_{l+1,m,i}^n$ , respectively, are the pressure values at two interpolated diagonal nodes lying on the sphere that goes through all eight diagonal grid points, as illustrated in Fig. 5(b). These interpolated nodes are equally distant from the boundary node  $p_{l,m,i}$  thus the stability condition for a family of compact explicit schemes is still obeyed. Since these interpolated values are located across the boundary, the discrete boundary condition in the direction normal to the wall can be applied, similarly to the procedure presented in [23]. Thus these three subconditions can be expressed as

$$p_{l+1,m,i}^n = p_{l-1,m,i}^n + \frac{a_0}{\lambda b_0}(p_{l,m,i}^{n-1} - p_{l,m,i}^{n+1}) + \frac{g_a^n}{b_0}, \quad (34)$$

$$\tilde{p}_{l+1,m,i}^n = \tilde{p}_{l-1,m,i}^n + \frac{a_0}{\lambda b_0}(p_{l,m,i}^{n-1} - p_{l,m,i}^{n+1}) + \frac{g_{sd}^n}{b_0}, \quad (35)$$

$$\bar{p}_{l+1,m,i}^n = \bar{p}_{l-1,m,i}^n + \frac{a_0}{\lambda b_0}(p_{l,m,i}^{n-1} - p_{l,m,i}^{n+1}) + \frac{g_d^n}{b_0}, \quad (36)$$

where  $g$  is an intermediate value in the filter updates for the respective subcondition, subscripts  $a$ ,  $sd$ , and  $d$  denote axial, side-diagonal and diagonal directions, respectively, and the boundary impedance filter is defined as

$$\xi_w(z) = \frac{b_0 + \sum_{i=1}^N b_i z^{-i}}{a_0 + \sum_{i=1}^N a_i z^{-i}}. \quad (37)$$

Substituting (30-33) into (34-36), and next applying all three boundary subconditions to eliminate for nine ghost points in the discrete wave equation (8), the overall boundary condition for the right boundary becomes

$$p_{l,m,i}^{n+1} = \left[ d_1(2p_{l-1,m,i}^n + p_{l,m+1,i}^n + p_{l,m-1,i}^n + p_{l,m,i+1}^n + p_{l,m,i-1}^n) + 2d_2(p_{l-1,m+1,i}^n + p_{l-1,m-1,i}^n + p_{l-1,m,i+1}^n + p_{l-1,m,i-1}^n) + d_2(p_{l,m+1,i+1}^n + p_{l,m+1,i-1}^n + p_{l,m-1,i+1}^n + p_{l,m-1,i-1}^n) + 2d_3(p_{l-1,m+1,i+1}^n + p_{l-1,m-1,i+1}^n + p_{l-1,m+1,i-1}^n + p_{l-1,m-1,i-1}^n) + d_4 p_{l,m,i}^n + \frac{\lambda^2}{b_0} g^n + \left( \frac{\lambda a_0}{b_0} - 1 \right) p_{l,m,i}^{n-1} \right] / \left( 1 + \frac{\lambda a_0}{b_0} \right), \quad (38)$$

where the impedance filter input  $x$ , filter output  $y$ , and the intermediate value  $g$  at time step  $n$  are respectively given by

$$x^n = \frac{a_0}{\lambda b_0}(p_{l,m,i}^{n+1} - p_{l,m,i}^{n-1}) - \frac{g^n}{b_0}, \quad (39)$$

$$y^n = \frac{1}{a_0}(b_0 x^n + g^n), \quad (40)$$

$$g^n = \sum_{i=1}^N (b_i x^{n-i} - a_i y^{n-i}). \quad (41)$$



In the derivation above, the superposition property of linear systems was applied to group the intermediate terms  $g_a$ ,  $g_{sd}$ , and  $g_d$  into one overall intermediate value  $g$ , as shown in [23] for the 2-D case. The DIF model requires updating (38-41) in the order of presentation.

### B. DIF Formulation for Boundary Edges and Corners

Similarly to the derivation presented in Section III-A, the update formulae for other boundaries, edges and corners can be derived. The left boundary update equation is obtained by removing minus in (27) due to the opposite flow direction, which leads to the boundary equations (38-41) with a difference that all pressure terms in (38) including subscript  $l-1$  are replaced with  $l+1$ . The boundary conditions in  $y$ - and  $z$ -directions follow directly from discretizing one of directional conditions

$$\frac{\partial p}{\partial t} = -c \xi_x \frac{\partial p}{\partial x}, \quad \frac{\partial p}{\partial t} = -c \xi_y \frac{\partial p}{\partial y}, \quad \frac{\partial p}{\partial t} = -c \xi_z \frac{\partial p}{\partial z} \quad (42)$$

and are easily obtained from (38-41) by swapping index terms for the respective direction in (38). The procedure for boundary edges and corners is always the same and consists of the following steps. Firstly, deciding on the number of boundary conditions that should be applied (with a maximum number of three), and next using linear interpolations for ghost points so that normal-incidence boundary conditions can be applied. Thus for an outer corner, three boundary conditions are required, two boundary conditions apply at outer edges, one at boundaries, and no boundary conditions are required for inner boundary edges and inner corners, respectively. Finally, such conditions with interpolated values are used to eliminate for all ghost points in the wave equation (8). Apart from linear interpolations, an additional condition that guarantees local coherence between meeting boundaries [34] holds at boundary edges and corners, which in a continuous form is respectively given as one of the following:

$$\frac{\partial p^2}{\partial x \partial y} = 0, \quad \frac{\partial p^2}{\partial x \partial z} = 0, \quad \frac{\partial p^2}{\partial y \partial z} = 0, \quad \frac{\partial p^3}{\partial x \partial y \partial z} = 0. \quad (43)$$

One of the first three conditions is applicable at a boundary edge, and in addition the last coherence condition holds at room corners. As an example, the formula for the top-right outer corner (see Fig. 5(c)), derived by applying all three boundary conditions (42) and four coherence conditions (43), is explicitly provided:

$$p_{l,m,i}^{n+1} = \left[ 2d_1(p_{l-1,m,i}^n + p_{l,m-1,i}^n + p_{l,m,i-1}^n) + 4d_2(p_{l-1,m-1,i}^n + p_{l-1,m,i-1}^n + p_{l,m-1,i-1}^n) + 8d_3 p_{l-1,m-1,i-1}^n + d_4 p_{l,m,i}^n + \lambda^2 \left( \frac{g_x^n}{b_x} + \frac{g_y^n}{b_y} + \frac{g_z^n}{b_z} \right) + \left( \frac{\lambda a_x}{b_x} + \frac{\lambda a_y}{b_y} + \frac{\lambda a_z}{b_z} - 1 \right) p_{l,m,i}^{n-1} \right] / \left( 1 + \frac{\lambda a_x}{b_x} + \frac{\lambda a_y}{b_y} + \frac{\lambda a_z}{b_z} \right), \quad (44)$$

where  $g_x$ ,  $g_y$ , and  $g_z$  are computed from their respective filter implementations,  $b_x$ ,  $b_y$ , and  $b_z$  are the filter  $b_0$  values, and  $a_x$ ,  $a_y$ , and  $a_z$  are the filter  $a_0$  values for the  $x$ -,  $y$ -, and  $z$ -direction boundary conditions, respectively. Hence the outer

corner requires updating three impedance filters (39-41) - one for each direction. Similarly, the formula for the outer edge can be derived by applying two boundary conditions (42) and one coherence condition (43), which for the  $x$ - $y$  outer edge yields

$$p_{l,m,i}^{n+1} = \left[ d_1(2p_{l-1,m,i}^n + 2p_{l,m-1,i}^n + p_{l,m,i+1}^n + p_{l,m,i-1}^n) + d_2(4p_{l-1,m-1,i}^n + 2p_{l-1,m,i-1}^n + 2p_{l-1,m,i+1}^n + 2p_{l,m-1,i-1}^n + 2p_{l,m-1,i+1}^n) + 4d_3(p_{l-1,m-1,i-1}^n + p_{l-1,m-1,i+1}^n) + d_4 p_{l,m,i}^n + \lambda^2 \left( \frac{g_x^n}{b_x} + \frac{g_y^n}{b_y} \right) + \left( \frac{\lambda a_x}{b_x} + \frac{\lambda a_y}{b_y} - 1 \right) p_{l,m,i}^{n-1} \right] / \left( 1 + \frac{\lambda a_x}{b_x} + \frac{\lambda a_y}{b_y} \right). \quad (45)$$

### C. Numerical Boundary Analysis

Similarly to dispersion analysis of FDTD schemes, an analytic formula for the numerical reflection for the DIF boundary model can be derived. Such a numerical boundary analysis (NBA) technique has been originally proposed in [29], and it is suitable for analytic prediction of reflection and proving the stability of correctly formulated boundary models. Applying the procedure presented in [30] for deriving the respective substitutions in (8), the NBA formula for the right-boundary reflectance reads

$$\hat{R}_{\theta,\phi}(z) = -\frac{Q - G A}{Q - G A^{-1}}, \quad (46)$$

where  $A = e^{j\hat{k}X \cos \theta \cos \phi}$ , the numerical wavenumber  $\hat{k}$  is computed from (23) combined with (18) for a given direction  $(\theta, \phi)$ , and the new variables are respectively given as

$$Q = \left( 1 + \frac{\lambda}{\xi_w(z)} \right) z + \left( 1 - \frac{\lambda}{\xi_w(z)} \right) z^{-1} - (d_1 D + d_2 E + d_4), \quad (47)$$

$$G = 2(d_1 + d_2 D + d_3 E), \quad (48)$$

$$D = (B + B^{-1} + C + C^{-1}), \quad (49)$$

$$E = (BC + B^{-1}C + BC^{-1} + B^{-1}C^{-1}), \quad (50)$$

where  $\xi_w(z)$  denotes the digital impedance filter,  $B = e^{j\hat{k}X \sin \theta \cos \phi}$ ,  $C = e^{j\hat{k}X \sin \phi}$ , and the implementation coefficients  $d_1$ - $d_4$  are given by (9).

The NBA formula is next used to prove the stability of the DIF boundary model by proving its passivity, which is a sufficient condition for the numerical stability of any numerical system [32]. Assuming single-frequency plane-wave solutions for any numerical wavenumber in the range  $-\pi/X \leq \hat{k} \leq \pi/X$ , (47) and (48) can be expressed respectively as

$$Q = \left\{ 2 \cos(\omega T) - 2d_1 [\cos(\hat{k}X \sin \theta \cos \phi) + \cos(\hat{k}X \sin \phi)] - 4d_2 \cos(\hat{k}X \sin \theta \cos \phi) \cos(\hat{k}X \sin \phi) + \frac{2\lambda b_w}{a_w^2 + b_w^2} \sin(\omega T) \right\} + j \left\{ \frac{2\lambda a_w}{a_w^2 + b_w^2} \sin(\omega T) \right\}, \quad (51)$$

$$G = 2 \left\{ d_1 + 2d_2 [\cos(\hat{k}X \cos \theta \sin \phi) + \cos(\hat{k}X \sin \phi)] + 4d_3 \cos(\hat{k}X \cos \theta \sin \phi) \cos(\hat{k}X \sin \phi) \right\}, \quad (52)$$

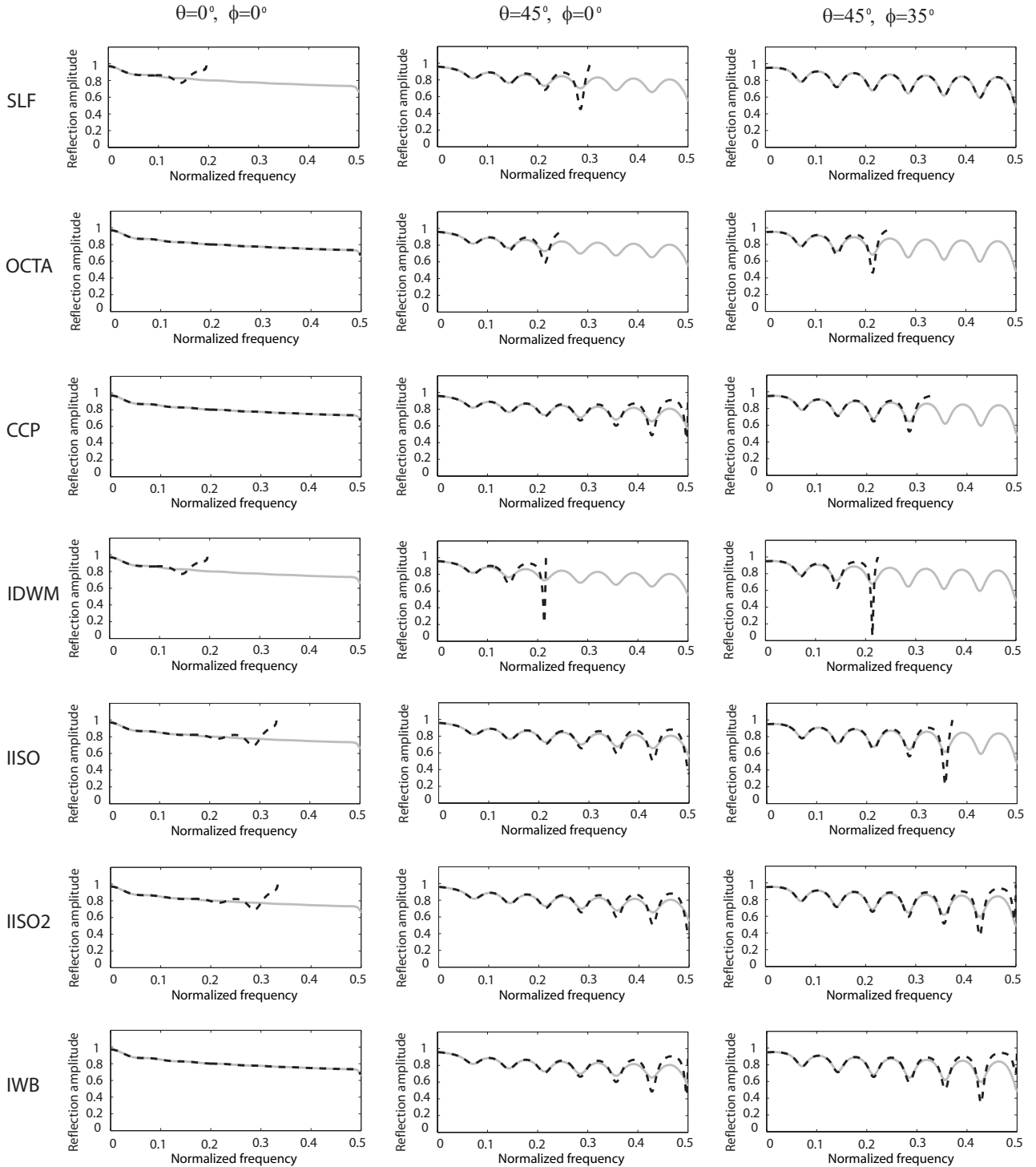


Fig. 6. Numerical reflection amplitude (dashed black lines) of the fibrous material boundary with  $d = 0.06$  and  $\sigma = 100$  compared with theoretical reflection amplitude (solid grey lines) for the following angles of incidence  $\theta = 0^\circ, \phi = 0^\circ$ ,  $\theta = 45^\circ, \phi = 0^\circ$ , and  $\theta = 45^\circ, \phi = 35^\circ$ .

where  $j = \sqrt{-1}$  and the complex-valued impedance for a specified frequency was represented by real and imaginary parts as  $\xi_w(z) = a_w + j b_w$ . The reflectance is passive when  $|\hat{R}_{\theta, \phi}(z)| \leq 1$ , which after simple algebraic manipulations (see [30] for details) leads to the following condition

$$-\sin(\hat{k}X \cos \theta \cos \phi) \text{Im}\{Q\}G \leq \sin(\hat{k}X \cos \theta \cos \phi)$$

$$\text{Im}\{Q\}G, \quad (53)$$

where  $\text{Im}\{Q\}$  denotes the imaginary part of  $Q$ . Since for all feasible parameter values (i.e.,  $-\pi/2 < \theta, \phi \leq \pi/2$  and frequencies up to Nyquist) it can be shown that  $\sin(\hat{k}X \cos \theta \cos \phi) \geq 0$ ,  $G \geq 0$ , and  $\sin(\omega T) \geq 0$ , it follows that the boundary is passive when  $a_w \geq 0$ . Thus the

boundary is passive (and hence the whole simulation stable) as long as the real part of the impedance is nonnegative, which is ensured for any digital impedance filter computed from a normal-incidence reflection filter using (29), for which  $|R_{0,0}(z)| \leq 1$ . Note that such a general stability proof using NBA technique is in essence similar to Von Neumann [15] and GKSO [35] analysis methods, and that analogous NBA formulae for corners and boundary edges can be derived, but are left out for brevity.

#### D. Reflection Analysis

This section presents the comparison of the magnitude of the numerical reflectance obtained from NBA with theoretical reflectance for 3-D DIF boundary models for schemes presented in Section II; example phase delay plots are also provided. Since the best and worst performance always results for one of the three extreme directions, the boundary analysis is restricted to the following angles of incidence: the normal incidence ( $\theta = 0^\circ$ ,  $\phi = 0^\circ$ ), the side-diagonal incidence ( $\theta = 45^\circ$ ,  $\phi = 0^\circ$ ), and the diagonal incidence ( $\theta = 45^\circ$ ,  $\phi = 35^\circ$ ). Firstly, the frequency-dependent results for an impedance filter representing the layer of fibrous material (following the design strategy described in Section III from analytic formulae given in [36]) for fibres thickness  $0.06m$  and flow resistivity  $100Nsm^{-4}$  are illustrated in Fig. 6. These plots are highly informative in assessing the cutoff frequencies for various incidences, which are shown to be the same as for the respective schemes. Thus for a given scheme, the frequency range in which the boundary reflections can be considered valid is equal to the valid frequency range for the room interior. Secondly, the phase delay of the numerical reflectance for two example boundary models is depicted in Fig. 7. Finally, the frequency range of accuracy (i.e., the bandwidth in which the relative numerical error does not exceed 2%) for frequency-independent boundaries (i.e., characterized by a real impedance) with the following impedance values  $\xi_w = 7/3, 4, 9$  and  $100$  are presented in Table III. These results indicate clearly that the numerical error in reflectance depends on the impedance value. For high impedance values (i.e., highly reflective boundaries), the error is small so that almost the whole simulation bandwidth can be effectively used, whereas for low impedance values the accuracy decreases. As shown in Table III, the performance for frequency-independent boundaries (i.e., scalar wall impedances) resembles closely the accuracy ranges and cutoff frequencies of the frequency-dependent results but, for brevity, no plots are shown here.

In general, the reflectance of the 3-D DIF boundary model matches theory closely for all angles of incidence and impedance values, which confirms its consistency with locally reacting surface theory. In particular, a perfect match in both phase and amplitude always results for low frequencies, whereas a complex-valued numerical error manifests itself in phase and amplitude at high frequencies. Comparing Figs. 6 and 7, the magnitude and phase delay plots behave similarly, i.e., in both cases the numerical error increases with frequency and the same numerical cutoff frequencies are displayed. Furthermore, a general observation can be made that the cutoff

TABLE III  
ACCURACY BANDWIDTH (2% RELATIVE ERROR IN REFLECTANCE) OF 3-D DIF BOUNDARIES FOR REAL IMPEDANCE VALUES  $\xi_w = 7/3, 4, 9, 100$ . THE VALID SIMULATION BANDWIDTH FOR THE BOUNDARY AND THE ACCURACY RANGE FOR THE ROOM INTERIOR ARE ALSO PROVIDED.

	SLF	OCTA	CCP	IDWM	IISO(2)	IWB
$\xi_w = 7/3$	0.066	0.089	0.143	0.057	0.147	0.153
$\xi_w = 4$	0.075	0.095	0.148	0.06	0.156	0.162
$\xi_w = 9$	0.096	0.122	0.181	0.074	0.188	0.199
$\xi_w = 100$	0.187	0.235	0.316	0.182	0.326	0.43
scheme acc.	0.075	0.093	0.175	0.069	0.175	0.186
bandwidth	0.196	0.25	0.333	0.196	0.333	0.5

frequencies of the 3-D boundary models for each direction are exactly the same as for the respective schemes, hence the values for  $f_a$ ,  $f_{sd}$ , and  $f_d$  provided for each scheme in Table I apply similarly to their respective boundary implementation. Furthermore, the reflectance error (averaged over a number of impedances) is roughly the same as the dispersion error for the respective scheme, and thus their accuracy and isotropy ranges can be considered equal. Note that a slightly higher error in reflectance (at low impedance values) is due to an additional discretization of derivatives in the boundary condition. Finally, as shown in Fig. 6 and Table III, the 3-D DIF IWB model is the most accurate and the IISO/IISO2 boundaries are the most isotropic for the widest frequency ranges.

#### IV. CONCLUSIONS

In this paper, a method for numerical modeling of room acoustics is presented, in particular FDTD techniques for simulating wave propagating in the room interior and reflections at the boundaries. A family of 3-D compact explicit schemes based on a nonstaggered rectilinear grid has been investigated, and the results indicate an improved performance of identified special cases in comparison to other approaches commonly found in FDTD and DWM literature on room acoustics. More specifically, the new 3-D interpolated wideband scheme and the 3-D interpolated isotropic schemes are indicated as the most efficient possible choices for accurate and isotropic FDTD simulations. The interpolated wideband model has the additional advantage of displaying no numerical error in directions where the most pronounced standing waves develop (i.e., between parallel walls). The identified isotropic models are shown to be highly efficient for a tight accuracy criterion, and - under the definition of a 2% isotropy error - are also shown to be isotropic for a wider frequency range than the 3-D interpolated digital waveguide mesh.

In addition, because the same scheme (approximating the wave equation) is applied across the medium, the boundaries, the edges, and the corners, consistency of scheme is realized across the simulation. This has so far not been the case for 3-D FDTD and digital waveguide mesh room acoustic simulations, apart from Botteldooren's room model [4]. Such consistency is not only crucial for ensuring stability, but also forms a prerequisite for rigorous numerical dispersion analysis

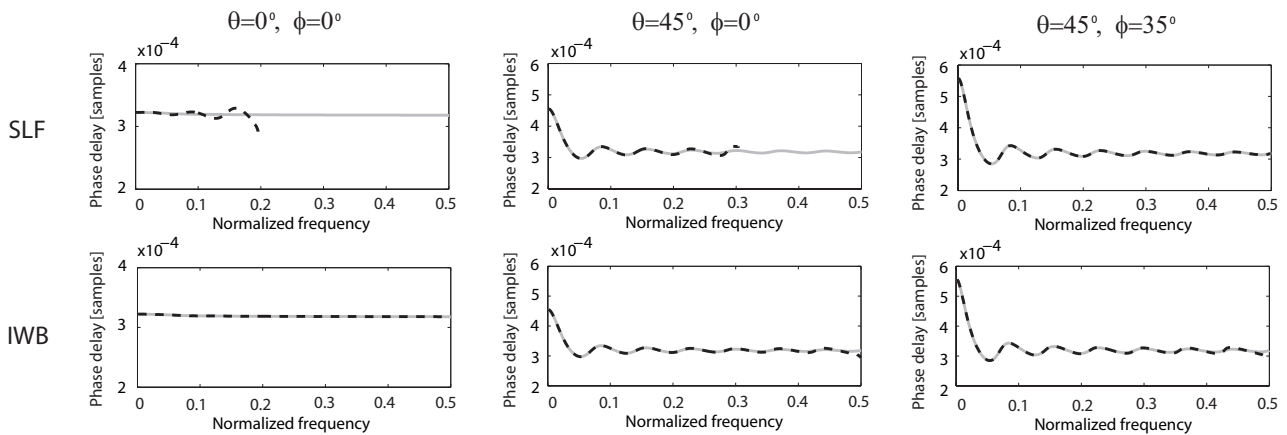


Fig. 7. Phase delay of the numerical reflection (dashed black lines) of the fibrous material boundary with  $d = 0.06$  and  $\sigma = 100$  compared with theoretical reflection phase delay (solid grey lines) for the SLF and the IWB schemes, and the following angles of incidence  $\theta = 0^\circ, \phi = 0^\circ, \theta = 45^\circ, \phi = 0^\circ$ , and  $\theta = 45^\circ, \phi = 35^\circ$ .

of all separate components of the simulation and indeed also to the ability to predict exactly how any numerical artifacts manifest themselves in calculated responses. One important consequence of this consistency is that frequency warping can for the first time be justifiably applied to responses obtained with FDTD or digital waveguide mesh simulations of rooms with realistic boundaries.

One aspect that has not been dealt with in this paper, and could be of interest for future research, is the comparison of the identified schemes with the tetrahedral topology [37], which is not captured within (2), or staggered-grid versions of the tetrahedral and octahedral topologies. However, the applicability of the tetrahedral stencil to room acoustic simulations is debatable due to the nontrivial formulation of boundary conditions for complex room shapes.

## REFERENCES

- [1] M. Kleiner, B.-I. Dalenbäck, and P. Svensson, "Auralization - an overview," *J. Audio Eng. Soc.*, vol. 41, no. 11, pp. 861–875, November 1993.
- [2] L. Savioja, J. Huopaniemi, T. Lokki, and R. Väinänen, "Creating interactive virtual acoustic environments," *J. Audio Eng. Soc.*, vol. 47, no. 9, pp. 675–705, 1999.
- [3] U.P. Svensson, "Modelling acoustic spaces for audio virtual reality," *Work. on Model based Proc. and Coding of Audio (MPCA)*, pp. 109–116, November 2002, Leuven, Belgium.
- [4] D. Botteldooren, "Finite-difference time-domain simulation of low-frequency room acoustic problems," *J. Acoust. Soc. Amer.*, vol. 98, no. 6, pp. 3302–3308, 1995.
- [5] J. Allen and D. Berkley, "Image method for efficiently simulating small-room acoustics," *J. Acoust. Soc. Amer.*, vol. 65, no. 4, pp. 943–950, April 1979.
- [6] A. Krokstad, S. Ström, and S. Sörnsdal, "Calculating the acoustical room response by the use of a ray tracing method," *J. Sound and Vibration*, vol. 8, no. 1, pp. 118–125, September 1968.
- [7] J. Borish, "An extension of the image model to arbitrary polyhedra," *J. Acoust. Soc. Amer.*, vol. 75, pp. 1827–1836, 1984.
- [8] S. Siltanen, T. Lokki, L. Savioja, and C. Christensen, "The room acoustic rendering equation," *J. Acoust. Soc. Amer.*, vol. 122, no. 3, pp. 1624–1635, 2007.
- [9] H. Kuttruff, *Room Acoustics*, Applied Science Publishers Ltd, London, 1973.
- [10] D.T. Murphy, M. Beeson, S. Shelley, A. Southern, and A. Moore, "RenderAIR room acoustics simulation using a hybrid digital waveguide mesh," *Proc. 124th AES Convention*, Preprint 7429, May 2008, Amsterdam, The Netherlands.
- [11] K.S. Yee, "Numerical solution of initial boundary value problems involving Maxwell's equations in isotropic media," *IEEE Trans. Antennas Propagat.*, vol. 14, pp. 302–307, 1966.
- [12] D. Botteldooren, "Acoustical finite-difference time-domain simulation in a quasi-cartesian grid," *J. Acoust. Soc. Am.*, vol. 95, no. 5, pp. 2313–2319, 1994.
- [13] G. Fairweather and A.R. Mitchell, "A new alternating direction method for the parabolic equations in the space variables," *J. Soc. Indust. Math. Appl.*, vol. 13, pp. 957–965, 1965.
- [14] K. Kowalczyk and M. van Walstijn, "On-line simulation of 2D resonators with reduced dispersion error using compact implicit finite difference methods," *Proc. IEEE Int. Conf. Acoust., Speech, Signal Process. (ICASSP)*, vol. 1, pp. 285–288, April 2007, Honolulu, Hawaii.
- [15] J.C. Strikwerda, *Finite Difference Schemes and Partial Differential Equations*, Wadsworth & Brooks, Pacific Grove, CA, 1989.
- [16] S. Bilbao, *Wave and Scattering Methods for Numerical Simulation*, John Wiley & Sons, London, 2004.
- [17] G.R. Campos and D.M. Howard, "On the computational efficiency of different waveguide mesh topologies for room acoustic simulation," *IEEE Trans. Speech Audio Process.*, vol. 13, no. 5, pp. 1063–1072, September 2005.
- [18] S. Bilbao and J.O. Smith, "Finite difference schemes and digital waveguide networks for the wave equation: Stability, passivity, and numerical dispersion," *IEEE Trans. Speech Audio Process.*, vol. 11, pp. 255–266, May 2003.
- [19] L. Savioja and V. Välimäki, "Interpolated rectangular 3-D digital waveguide mesh algorithms with frequency warping," *IEEE Trans. Speech Audio Process.*, vol. 1, no. 6, pp. 738–790, November 2003.
- [20] M. Karjalainen and C. Erkut, "Digital waveguide vs. finite difference schemes: Equivalence and mixed modeling," *EURASIP J. Applied Signal Processing*, no. 7, pp. 978–989, June 2004.
- [21] S. van Duyne and J.O. Smith, "The 2-D digital waveguide mesh," *Proc. IEEE Workshop Appl. Sign. Process. Audio, Acoust. (WASPAA)*, pp. 234–237, October 1993, Mohonk, NY.
- [22] M. van Walstijn and K. Kowalczyk, "On the numerical solution of the 2D wave equation with compact FDTD schemes," *Proc. Int. Conf. Digital Audio Effects (DAFx'08)*, pp. 205–212, September 2008, Espoo, Finland.
- [23] K. Kowalczyk and M. van Walstijn, "Wideband and isotropic room acoustics simulation using 2-D interpolated FDTD schemes," *IEEE Trans. Audio, Speech, Language Process.*, vol. 18, no. 1, pp. 78–89, January 2010.
- [24] L. Savioja, T. Rinne, and T. Takala, "Simulation of room acoustics with a 3-D finite difference mesh," *Proc. Int. Comp. Music Conf. (ICMC)*, pp. 463–466, September 1994, Aarhus, Denmark.
- [25] J. Huopaniemi, L. Savioja, and M. Karjalainen, "Modeling of reflections and air absorption in acoustical spaces - a digital filter design approach,"

- Proc. IEEE Workshop Appl. Sign. Process. Audio, Acoust. (WASPAA)*, pp. 1–4, October 1997, New Palz, NY.
- [26] A. Kelloniemi, “Frequency-dependent boundary condition for the 3-D digital waveguide mesh,” *Proc. Int. Conf. Digital Audio Effects (DAFx’06)*, pp. 161–164, September 2006, Montreal, Canada.
- [27] D.T. Murphy and M. Beeson, “The KW-boundary hybrid digital waveguide mesh for room acoustics applications,” *IEEE Trans. Audio, Speech, Language Process.*, vol. 12, no. 2, pp. 552–564, February 2007.
- [28] J. Escolano, F. Jacobsen, and J.J. López, “An efficient realization of frequency dependent boundary conditions in an acoustic finite-difference time-domain model,” *J. Sound and Vibration*, vol. 316, no. 1-5, pp. 234–247, 2008.
- [29] K. Kowalczyk and M. van Walstijn, “Formulation of locally reacting surfaces in FDTD/K-DWM modelling of acoustic spaces,” *Acta Acustica united with Acustica*, vol. 94, no. 6, pp. 891–906, December 2008.
- [30] K. Kowalczyk and M. van Walstijn, “Modeling frequency-dependent boundaries as digital impedance filters in FDTD and K-DWM room acoustics simulations,” *J. Audio Eng. Soc.*, vol. 56, no. 7/8, pp. 569–583, 2008.
- [31] A. Taflové and S.C. Hagness, *Computational Electrodynamics: The Finite-Difference Time-Domain Method, 2nd ed.*, Artech House, Norwood, MA, 2000.
- [32] J.O. Smith, *Physical Audio Signal Processing for Virtual Musical Instruments and Digital Audio Effects*, W3K Publishing, Available online: <https://ccrma.stanford.edu/jos/pasp>, August 2006.
- [33] J.W. Thomas, *Numerical Partial Differential Equations: Finite Difference Methods*, Springer-Verlag, New York, 1998.
- [34] M.E. McIntyre and J. Woodhouse, “On measuring the elastic and damping constants of orthotropic sheet materials,” *Acta Metallurgica*, vol. 36, no. 6, pp. 1397–1416, 1988.
- [35] B. Gustafsson, H.-O. Kreiss, and A. Sundström, *Time Dependent Problems and Difference Methods*, John Wiley & Sons, New York, 1995.
- [36] J.-F. Allard and Y. Champoux, “New empirical equations for sound propagation in rigid frame fibrous materials,” *J. Acoust. Soc. Amer.*, vol. 91, no. 6, pp. 3346–3353, 1992.
- [37] S.van Duyne and J.O. Smith, “The 3-D tetrahedral digital waveguide mesh with musical applications,” *Proc. Int. Comp. Music Conf. (ICMC)*, pp. 9–16, August 1996, Hong Kong.